Journal of Achievements in Materials and Manufacturing Engineering
VOLUME 37
ISSUE 2
December
2009

Effect of high power diode laser surface melting and cooling rate on microstructure and properties of magnesium alloys

L.A. Dobrzański *, T. Tański, J. Domagała, S. Malara, M. Król
Division of Materials Processing Technology, Management and Computer Techniques in Materials Science, Institute of Engineering Materials and Biomaterials, Silesian University of Technology, ul. Konarskiego 18a, 44-100 Gliwice, Poland
* Corresponding author: E-mail address: leszek.dobrzanski@polsl.pl

Received 18.09.2009; published in revised form 01.12.2009

Properties

ABSTRACT

Purpose: The goal of this paper is to present the investigation results of MCMgAl12Zn1, MCMgAl9Zn1, MCMgAl6Zn1, MCMgAl3Zn1 cast magnesium alloy in as-cast state and after heat treatment, as well as after laser treatment and thermal analysis during melting and solidification cycles carried out using the Universal Metallurgical Simulator and Analyser. In the following paper the structure and properties were presented of the above mentioned magnesium cast alloys in as-cast state and after a heat treatment.
Design/methodology/approach: A casting cycle of alloys was carried out in an induction crucible furnace using a protective salt bath Flux 12 was equipped with two ceramic filters at the melting temperature of 750±10°C, suitable for manufactured material. The following results concern scanning electron microscopy investigations in the SE observation mode, as well as using BSE modus for better phase contrast results, also quantitative microanalysis was applied for chemical composition investigations of the phases occurred.
Findings: The analysis of the samples after the ageing process has confirmed that the microstructure of the magnesium cast alloy consists of the solid solution α - Mg (matrix) of the secondary phase β - $Mg_{17}Al_{12}$ equally located in the structure. The roughness of the surface treatment layer was varied with laser power and also scan rate.
Research limitations/implications: According to the alloys characteristics, the applied cooling rate and alloy additions seem to be a good compromise for mechanical properties and microstructures, nevertheless, further tests should be carried out in order to examine different cooling rates and parameters of solution treatment process and ageing process.
Practical implications: A desire to create as light vehicle construction as possible and connected low fuel consumption made it possible to make use of magnesium alloys as constructional material in automotive industry.
Originality/value: The undertaken examinations aim at defining the influence of chemical composition and precipitation processes on the structure and casting magnesium alloy properties in its state and after heat treatment with a different content of alloy components.
Keywords: Heat treatment; Surface treatment; Magnesium cast alloys; Scanning electron microscope; Roughness

Reference to this paper should be given in the following way:
L.A. Dobrzański, T. Tański, J. Domagała, S. Malara, M. Król, Effect of high power diode laser surface melting and cooling rate on microstructure and properties of magnesium alloys, Journal of Achievements in Materials and Manufacturing Engineering 37/2 (2009) 238-257.

1. Introduction

In the last few decades the world noticed a rapid growth of application of magnesium and its alloys in almost every field of today's industry. This is due to numerous characteristics of the metal regarded to herein, which permit its use both as a structural element and as a chemical addition to other metal alloys. The metal is lighter than aluminum and has higher tensile strength than steel. Magnesium alloys have low density and other benefits are, such as: good vibration damping, high dimension stability, small casting shrinkage, connection of low density and huge strength with reference to small mass possibility to be applied in machines and use it easily in recycling process (Table 1) [1-4].

A widespread use of magnesium in structural applications is a collective dream of industry, although not everyone shares this vision. Magnesium alloys were widely used in structural applications during World War II and in a Volkswagen "Beetle" car in 1960s and 1970s. In the last decades, the obvious physical, chemical and mechanical advantages of magnesium allow for wide-range applications in miscellaneous spheres of modern industry. Nowadays, structural markets are considered to be the most important area of the future growth. [1-9].

Many obvious advantages offered by magnesium and its alloys are due to its special characteristics that put it out of comparison. The automotive industry has crossed the threshold from using magnesium in a protected environment, predominantly interior applications to an unprotected environment. Production magnesium components currently emphasize interior applications, such as steering column brackets, instrument panel, seat frames, steering wheel, and sunroof sliding track assembly etc (Fig.1) [1-9].

However, some modern applications expand magnesium's domain to roof panels, hood, rear deck lid, wheels, intake manifold, cylinder head cover, oil pan, starter/alternator, and engine block. Possibly the main technological reason that caused magnesium to be disadvantageous in respect to some competitive materials (plastic and aluminum) in the automotive industry is its corrosion properties. The latest technical developments help to avoid many key-issues related to magnesium expansion in the automotive. Considering its characteristics of low density, its extensive use in vehicles would obtain major reductions of weight and corresponding fuel savings. The data indicate that the overall weight savings could be of around 10%. In turn, this weight saving would lead to a fuel saving by about 20-30% without drastic changes in design. A new passenger car is produced at the average of some 150 g/km exhaust gasses. With magnesium technology this value could be reduced by around 100-120 g/km. Australian Magnesium Company announced a strategic alliance with German-based VAW Aluminium, AG to assess the potential for the production of a magnesium engine block. The agreement aims to define an appropriate engine block alloy, to test prototypes and move it to commercial production of a magnesium engine block. The annual demand for magnesium alloy in a typical mass-produced four-cylinder engine block is about 7000 t/a. AMC believes magnesium engine blocks will be used in a number of vehicles within the next 10 years [5-9].

In order to control microstructure development effectively when melting, solidification as well as further materials processing is necessary to understand all occurring metallurgical phenomena. Knowledge on solidification process as well as the influence of liquid and/or semi solid metal treatment on micro and macro structure characteristics is of primary importance. The samples and very effective method, which make it possible to determine a curve of the crystallization process – the cool curve $T=F(t)$,is thermal analysis. Advanced Thermal Analysis (TA) techniques monitor the temperature changes in sample as it is cooled down through a phase transformation interval [17-20]. The temperature changes in the materials are recorded as a function of heating or cooling time in such a manner that it allows to detect phase transformation. In order to increase accuracy, characteristic points on the cooling curve were identified using the first derivative curve plotted versus time [10-16].

Table 1.
Editorial requirements [1-4]

Stability of raw material cost and supply	Abundance of natural resources together with the cost effective primary processes contribute to a stable supply that can rapidly grow to meet future demands
Lower weight	Magnesium is the lightest structural metal. It is lighter than aluminium by 35 percent and lighter than zinc by 73 percent. Its excellent strength-to-weight ratio significantly decreases the weight and cost of magnesium components
Durability	magnesium is a durable metal with excellent capacity for damping vibrations
Machinability	magnesium is the easiest metal to machine, which leads to rapid processing and the cost effective production of finished parts
Perfect for complex application	in the die casting process magnesium can be formed into very complicated and thin-walled parts with a high degree of precision
Shielding against electromagnetic radiation	magnesium alloys, due to their excellent conductivity, shield against harmful electromagnetic radiation and are an ideal material to be used in electronic equipment, where electromagnetic radiation is an issue
Market growth	increase in the use of magnesium applications is approximately 15-20 percent annually

Increasing of surface layers properties can be achieved by many technologies i.e.: electroplating, anodizing, PVD, laser alloying or padding. Main advantages of laser treatment are like short time of process, flexibility or operation precision [24, 25].

The main goal of surface laser treatment is modification structure and properties. Increasing of wear resistance is to create results for chemically homogeneous, fine-crystalline surface layer without chemical changes. More advantageous properties can be achieved by alloying with hard particles of carbides, oxides or nitrides [24-26].

Laser technologies are the most promising and effective to provide continuous development of materials processing branch as results of forecasts concerning global economic development. One considers that economies which make use of laser technologies on a large scale, will be competitive on the global market [24-26].

A photographic camera casing

A computer casing

A phone casing

Roof structure

Back seat structure

Side seat structure

Steering Column Frame

Fig. 1. Elements from magnesium alloys

2. Experimental procedure

The investigations were carried out on test pieces of MCMgAl12Zn1 (Table 3, No. 1), MCMgAl9Zn (Table 3, No.2), MCMgAl6Zn (Table 3, No. 3), MCMgAl3Zn (Table 3, No. 4) magnesium alloys in as-cast and after heat treatment states made in cooperation with the Faculty of Metallurgy and Materials Engineering of the Ostrava Technical University and the CKD Motor plant, Hradec Kralove in the Czech Republic. The chemical compositions of the investigated materials are given in Table 3. A casting cycle of alloys was carried out in an induction crucible furnace using a protective salt bath *Flux 12* was equipped with two ceramic filters at the melting temperature of 750±10ºC, suitable for the manufactured material. In order to maintain a metallurgical purity of the melting metal, refining with neutral gas of the industrial name of *Emgesalem Flux 12* was carried out. To improve the quality of metal surface as a protective layer, *Alkon M62* was applied. The material was cast in dies with betonite binder because of its excellent sorption properties and shaped in plates of 250x150x25 mm. The cast alloys were pre-heated in an electrical vacuum furnace *Classic 0816 Vak* in protective argon atmosphere.

Table 2.
Parameters of investigated alloy heat treatment

Sing of heat treatment state	Conditions of solution heat treatment		
	Temperature °C	Heating time, h	Cooling method
0	As-cast		
	Solution treatment		
1	430	10	Water
2	430	10	Air
3	430	10	In furnace
	Aging treatment		
4	190	15	Air

Table 3.
Chemical composition of investigated alloy

	The mass concentration of main elements, %						
No.	Al	Zn	Mn	Si	Fe	Mg	Rest
1	12.1	0.62	0.17	0.047	0.013	86.96	0.0985
2	9.09	0.77	0.21	0.037	0.011	89.79	0.0915
3	5.92	0.49	0.15	0.037	0.007	93.33	0.0613
4	2.96	0.23	0.09	0.029	0.006	96.65	0.0361

2.1. Thermal analysis of cast magnesium alloys

The alloys were cast into bars of approximately 1.68kg mass. Next the material was prepared mechanically to a form like it is shown in Figure 2.

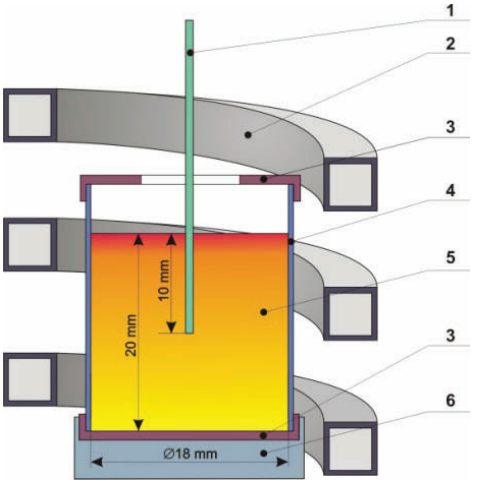

Fig. 2. Scheme of the UMSA Thermal Analysis Platform experimental set-up: 1 – low thermal mass thermocouple, 2 – heating and cooling coil, 3 – thermal insulation, 4 – steel foil, 5 – test sample, 6 – ceramic base

The thermal analysis during melting and solidification cycles was carried out using the Universal Metallurgical Simulator and Analyser (UMSA) (Fig. 3) [3-5]. The samples with dimensions were pre-heated to the temperature 700±1°C by generator of about 5 kW power. The melting and solidification experiments of the cast magnesium alloys were carried out using Argon as shielding gas.

The cooling rates for these experiments were determined using the following formula:

$$CR = \frac{T_{Liq} - T_{Sol}}{t_{Sol} - t_{Liq}} \left(\frac{^{\circ}C}{s} \right) \quad (2.1)$$

where T_{liq} and T_{Sol} are the liquidus and solidus temperatures (°C), respectively, and t_{liq} and t_{sol} are the times from the cooling curve that correspond to liquidus and solidus temperatures respectively [1, 2].

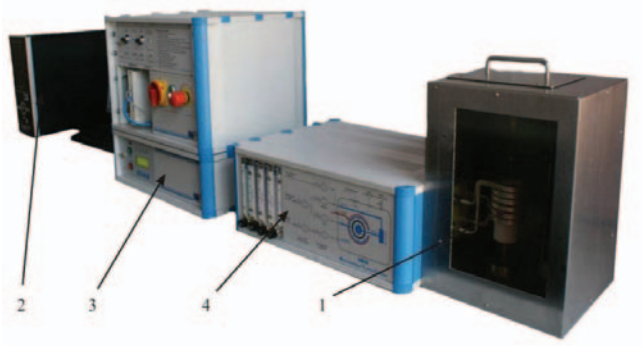

Fig. 3. UMSA apparatus, 1 – sample chamber, 2 – supervisory computer, 3 – temperature control, 4 – gas flow control

To achieve an intentional cooling rate:
- ≈ 0.6°C/s sample was cooled by air
- ≈ 1.2°C/s sample was cooled in airflow 30 l/min,
- ≈ 2.4°C/s sample was cooled in airflow 125 l/min.

A supersensitive K type thermocouple (with extra low thermal time constants) positioned at the centre of the test sample to collect the thermal data and control the processing temperatures. For one cooling rate measurement, one thermocouple was used. Every measurement was repeated five times to estimate results. To determine a relationship between temperature, time and characteristics parameters of processes proceeded during solidification i.e. liquidus, solidus and eutectic temperatures, each trial was repeated three times. To date handling OriginLab Pro 8 with Savitzky-Golay method was used.

Methodology determining characteristics parameters from thermal-derivation analysis

Fraction solid (FS) was determined by calculating the cumulative surface area between the first derivative of the cooling curve and the so-called base line (BL). The BL represents the hypothetical first derivative of the cooling curve that does not exhibit phase transformation /metallurgical reactions during the solidification process. The area between the two derivative curves (calculated between the liquidus and solidus temperatures) is proportional to the latent heat of solidification of a given alloy. Therefore, the latent heat directly delivered to the test sample affected the fraction liquid evolution. Similar calculations were performed for the fraction solid except that fraction solid was proportional to the latent heat released during the solidification [19, 21-23].

Table 4.
Characteristic points obtained from thermal-derivative analysis

Point	Temperature	Time	Description
I	T_{DN}	t_{DN}	Nucleation of α-phases (liquidus temperature)
II	T_{Dmin}	t_{Dmin}	The α-Mg dendrite minimum (undercooling) temperature
III	T_{DKP}	t_{DKP}	Coherency point
IV	T_G	t_G	The α-Mg dendrite growth temperature
V	$T_{(Mg+Si+Al+Mn)}$	$t_{(Mg+Si+Al+Mn)}$	Crystallisation of α-Mg, Mg_2Si and phases contains Al and Mn
VI	$T_{(Mg+Si+Al+Mn)f}$	$t_{(Mg+Si+Al+Mn)f}$	End of crystallisation of Mg_2Si and phases contains Al and Mn
VII	$T_{E(Mg+Al)N}$	$t_{E(Mg+Al)N}$	Beginning of nucleation of α(Mg)+β(Mg-$Mg_{17}Al_{12}$) eutectic
VIII	$T_{E(Mg+Al)min}$	$t_{E(Mg+Al)min}$	The α(Mg)+β(Mg-$Mg_{17}Al_{12}$) minimum (undercooling) temperature
IX	$T_{E(Mg+Al)G}$	$t_{E(Mg+Al)G}$	The α(Mg)+β(Mg-$Mg_{17}Al_{12}$) eutectic growth temperature
X	T_{sol}	t_{sol}	End of solidification (solidus temperature)

Representative cooling, crystallisation and calorimetric curves with characteristics points of crystallization process of MC MgAl9Zn1 alloy was presented in Figs. 4, 5. Description of characteristics points obtained from thermal-derivative analysis was presented in Table 4.

Based on characteristics points from the thermal analysis, heat of phase transition individual phases was calculated. Temperatures and times of thermal processes were calculated as well.

Heat capacity of the alloy was determined using the following formula:

$$c_p(t) = c_{p_{sol}} \cdot \int_{t_N}^{t} f_s(t)dt + c_{p_{Liq}} \cdot \left(1 - \int_{t_N}^{t} f_s(t)dt\right) \quad (2.2)$$

where:
f_s – participation of fraction solid, considering that for $f_s(t \le t_N)= 0$ and $f_s(t \ge t_N)= 1$.
Thermal-Calc Software was used to determine a specific heat capacity in liquid and solid state.

Total heat of crystallization process of analyzed alloys was calculated based on:

$$Q = c_p \cdot m \cdot \int_{t_N}^{t_{sol}} \left[\frac{dT}{dt} - \left(\frac{dT}{dt}\right)_c\right] \quad (2.3)$$

2.2. Laser treatment

Plates were polished with 1200-grit SiC paper prior to laser surface treatment to obtain smooth surface and then cleaned with alcohol and dried up.

Seven types of powders were used in present study for alloying process, namely, tungsten, titanium, vanadium, silicon, niobium, tantalum carbides and aluminium oxide (Table 5).

Laser alloying was made using the Rofin DL020 HPDL high power diode laser in the argon shield gas cover to protect the molten metal pool from oxidation with the technique of the continuous powder supply to the remelted pool area, by feeding the granulate using the TecFlo fluidisation feeder equipped with the powder flow digital controller. Powder feeder was connected with the transport gas cylinder and powder feed nozzle (Fig. 6). Gas feed rate was 5 [l/min].

The laser alloying of magnesium alloys was conducted by remelting Mg-Al-Zn surface and feeding of carbides or oxides particles performed by high power laser diode HPDL Rofin DL 020 under argon shielding gas. The parameters are presented in Table 6.

Argon was used during laser re-melting to prevent the coating and the substrate from oxidation. Prior to approach a laser treatment, powders were desiccated in the furnace at the temperature of 100°C.

Experiments were made at the following process parameters: laser power 1.2 – 2.0 kW; alloying feed rate 0.50 – 1.00 m/min; powder feed rate: 6-9 g/min. After initial experiments laser power in the range 1.2-2.0 kW was assumed for the investigations, with alloying feed rates of 0.25; 0.50; 0.75; 1.00 m/min. The examinations revealed that the optimum geometry of a single laser path was obtained for alloying with the feed rate of 0.75 m/min. However, for laser treatment with powder injection of Al_2O_3 and NbC powders the optimum feed rate was 0.50 m/min and 0.25 m/min, respectively.

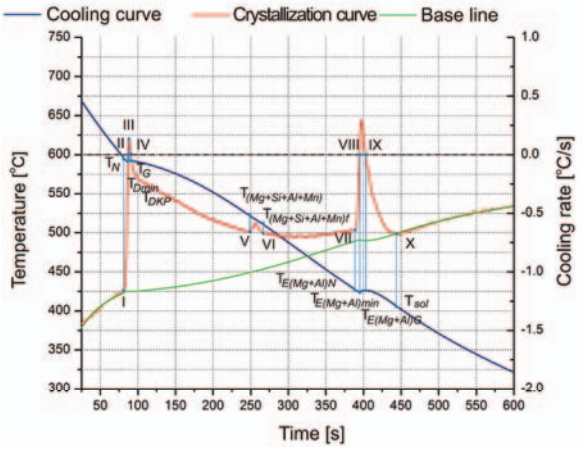

Fig. 4. Representative cooling and first derivative vs. temperatures curves recorded during the solidification cycles of MC MgAl9Zn1 alloy that was solidified at the rate 0.6°C/s

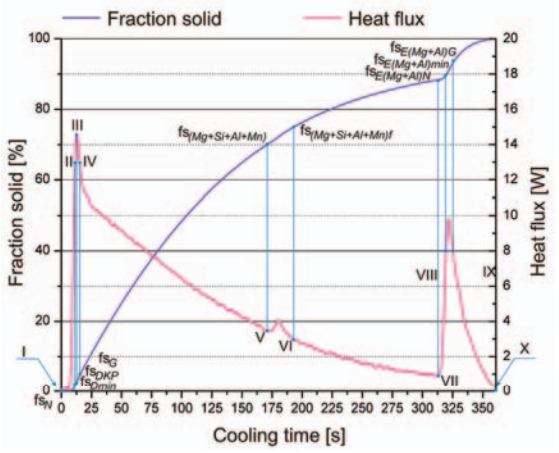

Fig. 5. Representative curves presented changes of heat flux and fraction solid of MC MgAl9Zn1 alloy that was solidified at the rate 0.6°C/s

Metallographic examinations were made on magnesium cast alloy specimens inserted in thermohardening resins. In order to disclose grain boundaries and the structure and to distinguish precisely the particular precipitations in magnesium alloys as an etching reagent 5% molybdenic acid was used. The observations of the investigated cast materials were done on the light microscope LEICA MEF4A as well as on the electron scanning microscope Opton DSM-940 and ZEISS Supra 35.

Table 5.
Properties of ceramic powders used for alloying process

Property	WC	TiC	VC	NbC	SiC	TaC	Al_2O_3
Density, kg/m^3	15.69	4.25	5.36	7.60	3.44	15.03	3.97
Hardness, HV	3400	1550	2850	2100	1600	1725	2300
Melting temperature, ^{o}C	2870	3140	2830	3500	1900	3880	2047
Average size grain, µm	0.7-0.9	< 1.0		<10	<10	<10	1-5
	>5	>6.4	>1.8	<45	<75	<45	80

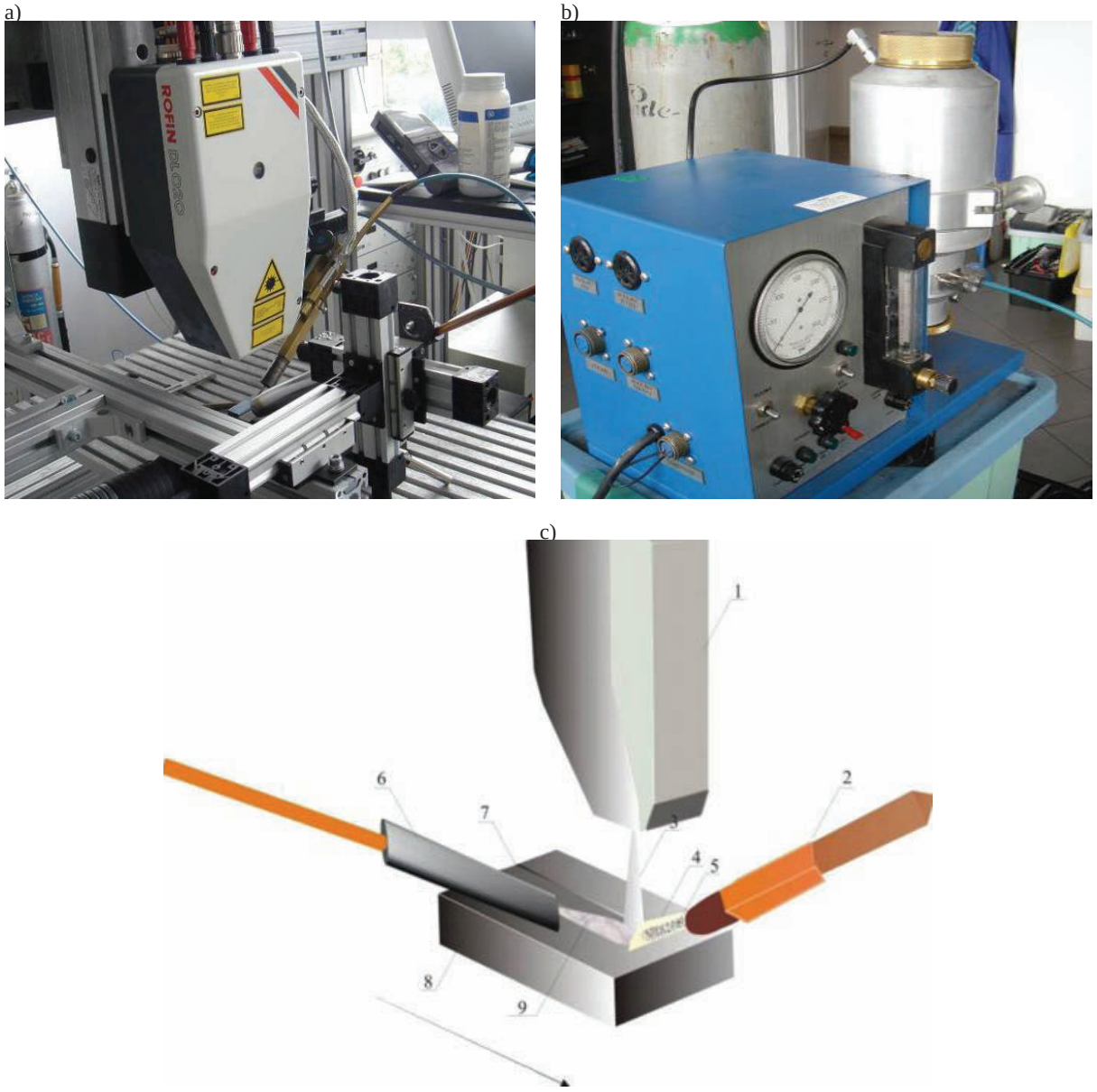

Fig. 6. a) Laser HPDL Rofin DL 020, b) feeder, c) scheme of laser treatment process of cast magnesium alloys: 1-laser head, 2- transport gas cylinder and powder feed nozzle, 3-beam laser, 4-gas, 5-powder, 6- powder feed nozzle, 7-remelting zone, 8-base material, 9-protective gas

Table 6.
HPDL Rofin DL 020 parameters

Laser wave length, nm , nm	808 - 940
Focus length of the laser beam, mm	82
Power density range of the laser beam in the focus plane [kW/cm^2]	0.8 - 36.5
Dimensions of the laser beam focus, mm	1.8 x 6.8

The X-ray qualitative microanalysis and the analysis of a surface distribution of cast elements in the examined magnesium cast alloy specimens were made on transverse micro-sections on the Opton DSM-940 and ZEISS Supra 35 scanning microscope with the Oxford EDS WDS dispersive radiation spectrometer at the accelerating voltage of 15 kV.

Roughness measurements of surface layers of laser alloyed cast alloys were performed on Taylor Hobson Precision Surtronic 3+. Measuring device is characterized by measuring resolution 0.2 µm and measuring range to 150 µm. Measurements were made on distance 0.8 mm.

Model of neural network was used to verify correctness of experimental roughness measurements. The feed forward neural networks were applied for calculations – Multi Layers were applied for calculations – Multi Layerceptron (MLP). The number of nodes in input was defined as four, which correspond to alloyed powder type (nominal variable), aluminium concentration in the alloy, laser power and alloying speed. Number of nodes in output layer was defined as one – roughness Ra (Fig. 7). One-of-N conversion type was applied for nominal variable and mini/max conversion for other variables. One-of-N conversion types using neurons number answers one nominal variable that is equal to a number of values achieved by this variable. In order to represent selected variable, appropriate neuron is activated and the rest of then remain inactive.

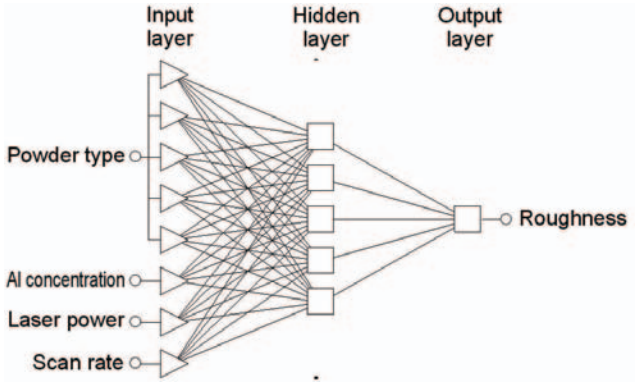

Fig. 7. Scheme of MLP neural network calculates roughness

Data set was divided into three subsets: training (61 cases), validating (22 cases) and testing (22 cases) ones. The result of design and optimisation process is a network, which is characterised by an error of value, standard deviation and Pearson's correlation coefficient.

The number of hidden layers, number of nodes in these layers and the number of training epochs were determined by observing the neural prediction error for the training and validating sets. Neural network training was carried with error back propagation method and conjugate gradient algorithm.

The neural network with one hidden layer and numbers of neurons in this layer as 5 was assumed to be optimal. The highest value of Pearson's correlation coefficient and the lowest value of standard deviation were achieved for MLP neural network that was trained by error back propagation method in 50 epochs and conjugate gradient algorithm in 59 epochs. The characteristic that was a base of valuation was presented in Table 7.

Table 7.
Regression statistics of neural network calculating roughness value in data sets

	Data set		
	Training	Validating	Testing
Error, Ra	1.99	1.68	1.53
Standard deviation	0.42	0.41	0.42
Pearson's correlation coefficient r	0.91	0.91	0.91

Pearson's correlation coefficient r equal 0.91 for three data sets: training, validating and testing and quotients of standard deviation, which are higher than 0.43 for three data sets indicate on roughness Ra prediction freedom from bias (Fig. 8).

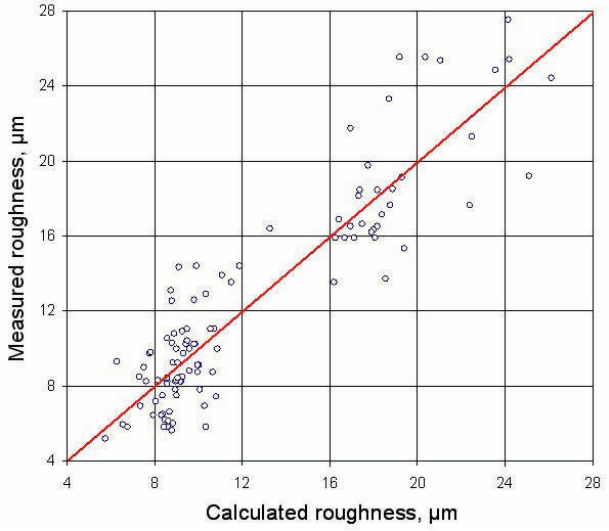

Fig. 8. Real roughness value and calculating value comparison for all test data sets

Regression function, which approximate dependence between output variable Y (roughness Ra) and input variables Xi (for instance aluminium contain, laser power, alloying speed) was also determined. The most often model applied in technological investigations was a use of [27]:

$$Y(X)=\beta_o+\sum_{i=1}^{L}\beta_i X_i+\sum_{i=1}^{L-1}\sum_{j=i+1}^{L}\beta_{ij}X_iX_j+\sum_{i=1}^{L}\beta_{ii}X_i^2,$$

for $L \geq 2$, (2.4)

where:

$\hat{Y}(X)$ – value of regression function for input variables vector $X=[X_1, X_2 \ ...X_L]^{T,}$

β_i, β_{ij} - coefficients of regression function, calculated by the least square method,

L – input variable number.

Regression function consists of the following parts: constant – coefficient β_0, linear – first sum, interaction – double sum and square – last sum.

Regression models were developed in RSTOOL computer application, which is an element of Statistic Toolbox packet of MATLAB environment. Input data were:

- Matrix of input variable values vector X^T_{ij}, for i = 1..L and j=1..M, M-measurements number,
- Output variable value Y_j, measurement results,
- Regression function model type,
- significance level for confidence interval for forecast value $\hat{Y}(X)$.

Coefficient of regression function, and cross-section of regression function graphs in planes, which were specified by input variable values, had been the result of analysis. Multidimensional correlation coefficient was a base for evaluation of quality of regression function [27]:

$$R=\left(\frac{\sum\left(Y\left(X_{ij}\right)-\overline{Y}\right)^2}{\sum_{j=1}^{M}\left(Y_j-\overline{Y}\right)^2}\right)^{\frac{1}{2}},$$ (2.5)

where:

$Y\left(X_{ij}\right)$ - regression function value for input variables vector, for j measurement,

$\overline{Y}$ - output variable values mean,

Y_j - result of j measurement of output variable.

Coefficient R values are in the range from 0 to 1, where 0 means correlation lack. Correlation coefficient significance was calculated according to formula [27]:

$$F=\frac{(M-L)R^2}{(L-1)(1-R^2)}$$ (2.6)

Correlation coefficient is significant on α level, if F coefficient is higher than Fischer-Snedecora distribution critical value for determined significant level and numerator and denumerator degree of freedom, which equal suitably $(L-1)$ and $(M-L)$.

Significant correlation coefficient was calculated by FPDF function, which is an element of Statistic Toolbox packet of MATLAB environment. This function calculates probability value of specified random variable with F distribution value occurrence for determined numerator and denumerator degree of freedom [27].

3. Discussion of experimental results

3.1. Thermal-derivative analysis

Figures 9-16 present microstructures obtained on light optical microscope. The MCMgAl3Zn1, MCMgAl6Zn1, MCMgAl9Zn1, MCMgAl12Zn1 alloys are characterised by microstructure of the solid solution α constituting the alloy matrix as well as the β – $Mg_{17}Al_{12}$ discontinuous intermetallic phase in the forms of plates located mostly at grain boundaries. Moreover, in the vicinity of the β intermetallic phase precipitations the presence of the needle eutectics (α + β) was revealed. In the structure of the examined magnesium cast alloys one can observe, apart from $Mg_{17}Al_{12}$ precipitations, turning grey phases, characterised by angular contour with smooth edges in the shape of hexahedrons. Out of the chemical composition examinations with the use of the EDS dispersive radiation spectrometer as well as literature data, one can conclude that it is the Mg_2Si compound which, when precipitating, increases the hardness of castings.

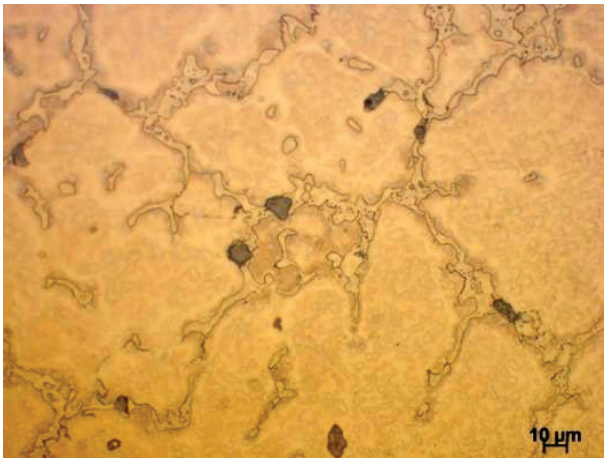

Fig. 9. Micrographs of the MCMgAl3Zn1 that was solidified at the rate 2.4°C/s

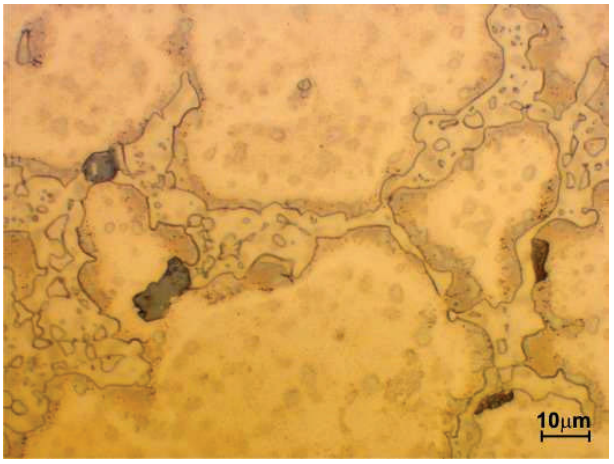

Fig. 10. Micrographs of the MCMgAl3Zn1 that was solidified at the rate 2.4°C/s

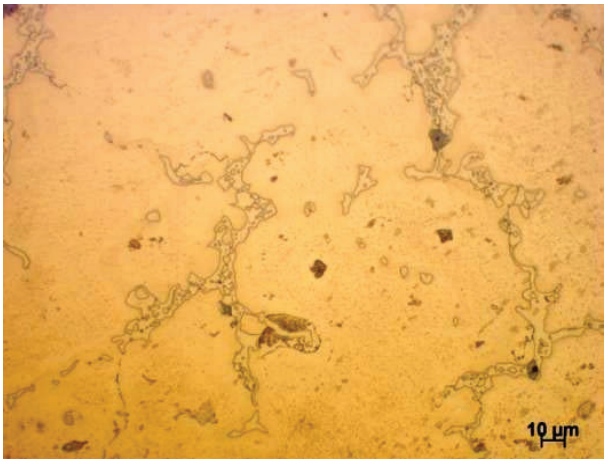

Fig. 11. Micrographs of the MCMgAl6Zn1 that was solidified at the 2.4°C/s

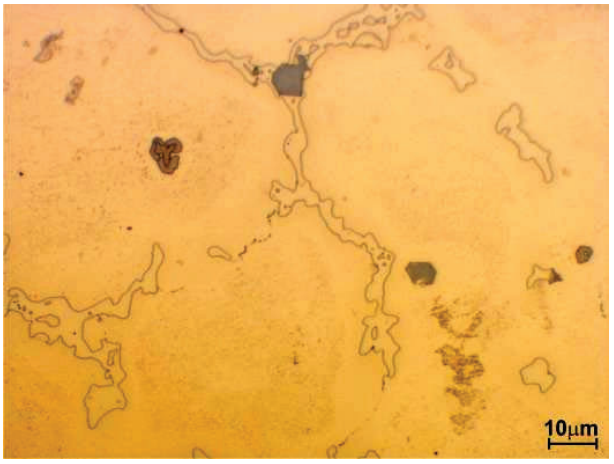

Fig. 12. Micrographs of the MCMgAl6Zn1 that was solidified at the rate 2.4°C/s

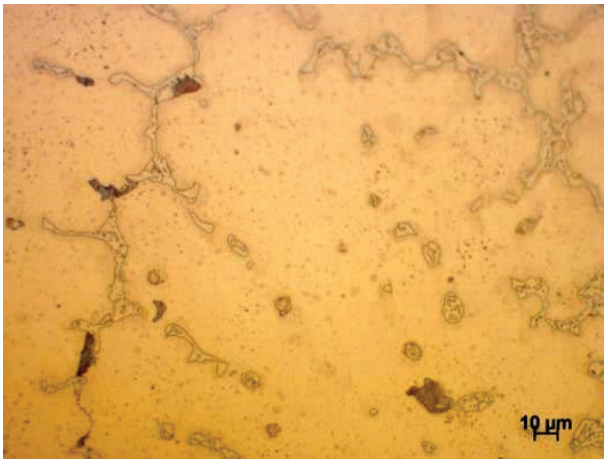

Fig. 13. Micrographs of the MCMgAl9Zn1 that was solidified at the 2.4°C/s

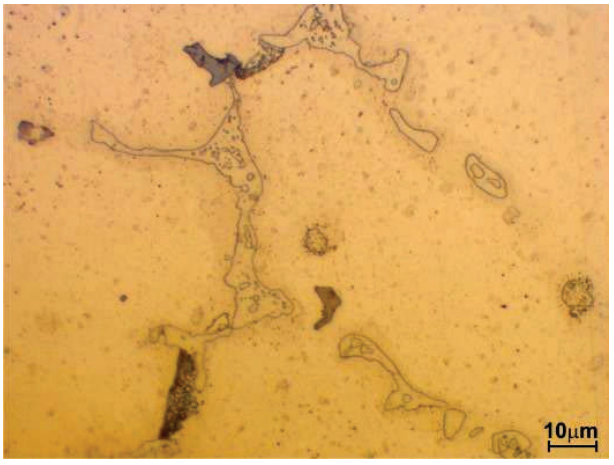

Fig. 14. Micrographs of the MCMgAl9Zn1 that was solidified at the 2.4°C/s

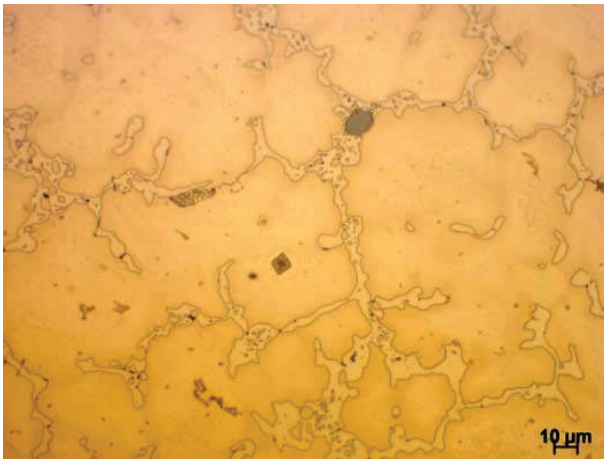

Fig. 15. Micrographs of the MCMgAl12Zn1 that was solidified at the rate 2.4°C/s

Fig. 16. Micrographs of the MCMgAl12Zn1 that was solidified at the rate 2.4°C/s

The quantitative micro analysis made on the transverse micro- sections of the magnesium alloys using the EDS system have confirmed the evident concentrations of silicon, aluminium and manganese what suggests the occurrence of precipitations containing Mg and Si with angular contours in the alloy structure as well as phases with high Mn and Al concentrations that are irregular with a non plain surface, often occurring in the forms of blocks or needles (Fig. 17 and 21). Figures 18-20 and 22-24 present EDS spectra of representatives Mg alloys after thermal analysis.

Investigation of microstructure, literatures and values from equilibrium systems allowed to determine a sequence of reaction proceeded during solidification of Mg-Al-Zn alloys:

1. $L \rightarrow \alpha(Mg)$
2. $L \rightarrow \alpha(Mg)+Mg_2Si+(Al+Mn)$
3. $L \rightarrow \alpha(Mg)+\beta(Mg - Mg_{17}Al_{12})$

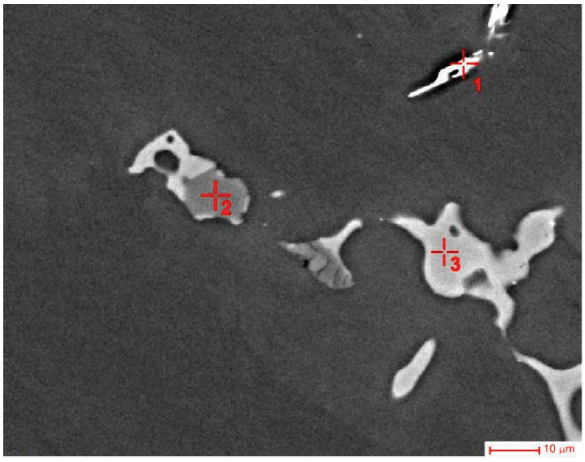

Fig. 17. SEM/BSD microstructure of the MCMgAl6Zn1 that was solidified at the rate 0.6°C/s

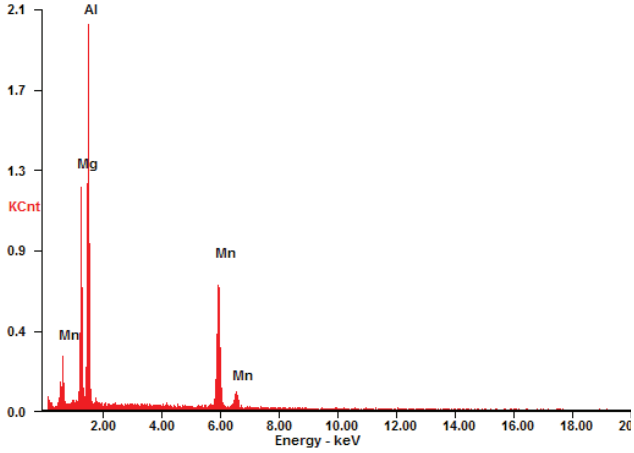

Fig. 18. EDS spectra of the MCMgAl6Zn1 that was solidified at the rate 0.6°C/s – analysis 1

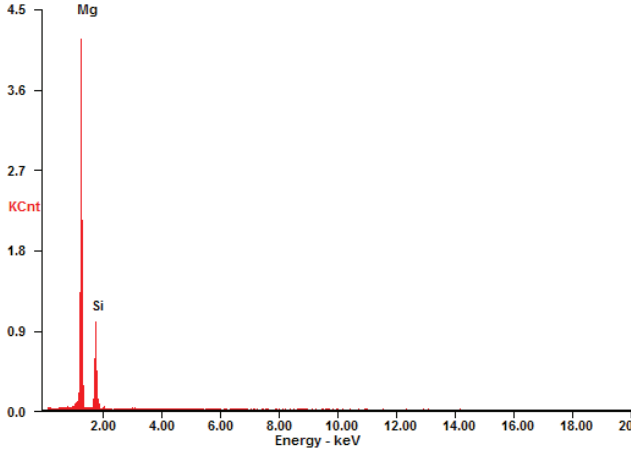

Fig. 19. EDS spectra of the MCMgAl6Zn1 that was solidified at the rate 0.6°C/s – analysis 2

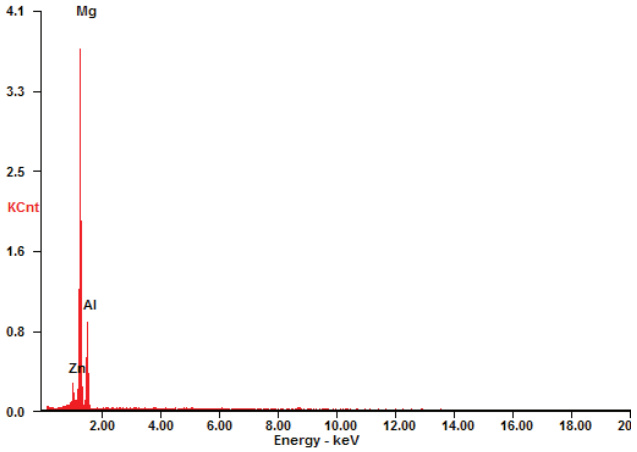

Fig. 20. EDS spectra of the MCMgAl6Zn1 that was solidified at the rate 0.6°C/s – analysis 3

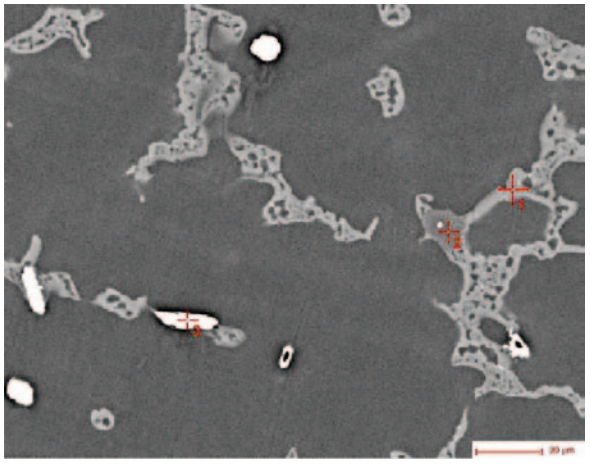

Fig. 21. SEM/BSD microstructure of the MCMgAl12Zn1 that was solidified at the 2.4°C/s

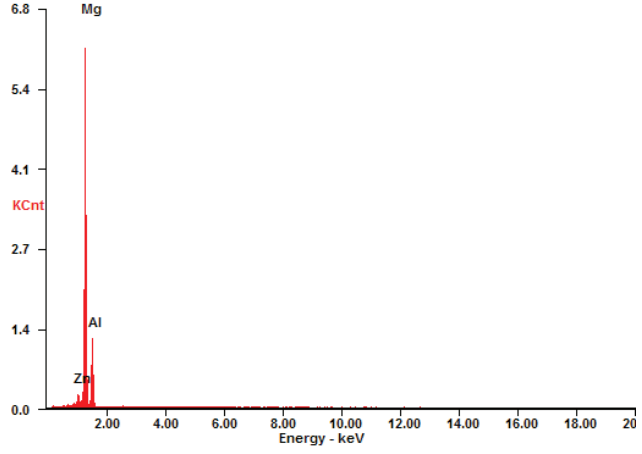

Fig. 22. EDS spectra of the MCMgAl12Zn1 that was solidified at the rate 2.4°C/s – analysis 1

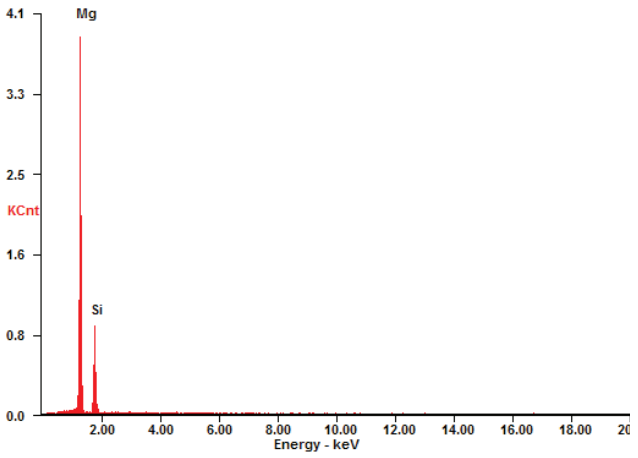

Fig. 23. EDS spectra of the MCMgAl12Zn1 that was solidified at the rate 2.4°C/s – analysis 2

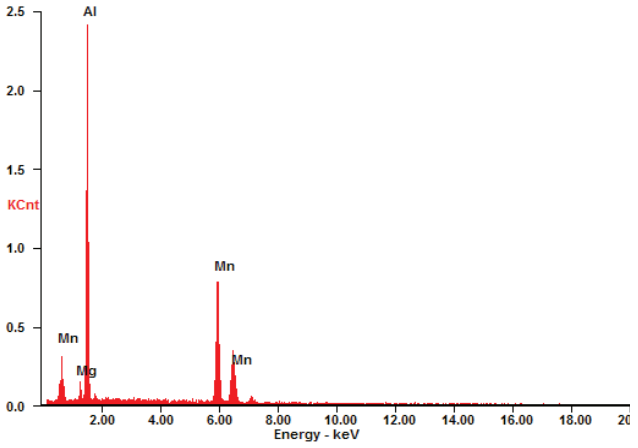

Fig. 24. EDS spectra of the MCMgAl12Zn1 that was solidified at the 2.4°C/s – analysis 3

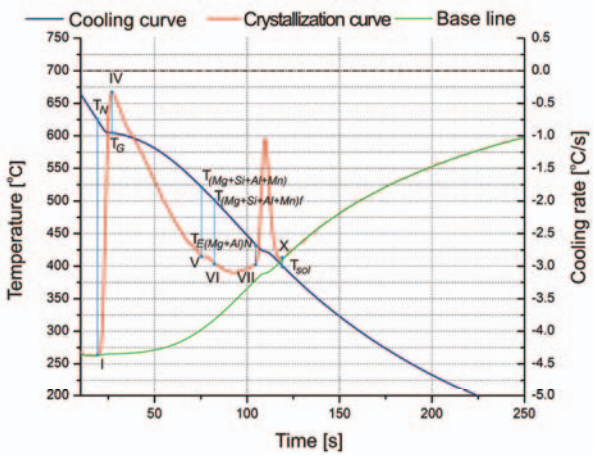

Fig. 25. Representative cooling, crystallization and calorimetric curves of the MCMgAl6Zn1 that was solidified at the 2.4°C/s

Representative thermal analyses of MC MgAl6Zn1 alloy were presented in figure 25. Few visible temperature arrests were noted on the cooling curves. More detailed information pertaining to the alloy's thermal characteristics such as non-equilibrium liquidus, nucleation of the α(Mg)-β($Mg_{17}Al_{12}$) eutectic, etc. were determined using the first derivative curves. The temperatures of the metallurgical reactions are presented in Table 8. Based on the cooling curve analysis, the non-equilibrium liquidus temperature of MC MgAl6Zn1 alloy that solidified under 0.6°C/s was found approximately 618.9°C. At 428.3°C the next change in the first derivative curve was observed and corresponded to the nucleation of the α(Mg)-β($Mg_{17}Al_{12}$) eutectic. It was found that non-equilibrium solidus temperature was approximately 417.1°C

Table 8.
Non-equilibrium thermal characteristics of the MC MgAl6Zn1 alloy test samples obtained during the solidification process at 0.6°C/s, 1.2°C/s and 2.4°C/s solidification rates

Characteristic point	Solidification rates [°C/s]		
	0.6	1.2	2.4
	Temp. [°C]	Temp. [°C]	Temp. [°C]
I	618.9±3.04	618.2±0.6	617±1.2
VII	428.3±0.47	429±1.2	435.4±1.9
X	417.1±1.3	412.7±3.3	405.8±2.4

The non-equilibrium liquidus temperature of MC MgAl6Zn1 alloy that solidified under a 1.2°C/s was found approximately 618.2°C. The nucleation of the α(Mg)-β($Mg_{17}Al_{12}$) eutectic was observed at 429°C.

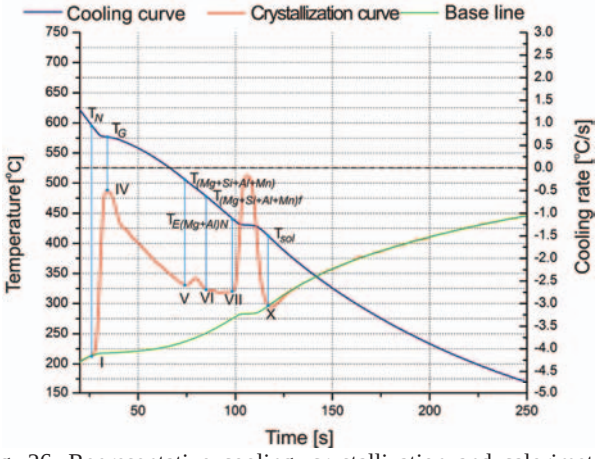

Fig. 26. Representative cooling, crystallization and calorimetric curves of the MC MgAl12Zn1 that solidified with rate 2.4°C/s

The solidification sequence of the MC MgAl6Zn1 alloy finished when the solidus reaction was completed at 412.7°C. Based on the first derivative of the cooling curve analysis, the liquidus temperature of the alloy solidified fewer than 2.4°C/s was found at 617°C. The nucleation of the α(Mg)-β($Mg_{17}Al_{12}$) eutectic was observed at 435.4°C. The solidification process was finished approximately 405.8°C. Changes of liquidus temperature are not observed during the examination, this temperature is constant for all cooling rates. The α+β eutectic nucleation temperature increase along with cooling rate increase from 0.6 to 2.4 °C/s, the α+β eutectic nucleation temperature increases from approximately 428.3 to 435.4°C. Due to the increase of the cooling rate the solidus temperatures decrease. When the cooling rate is increased, the solidification range is increased from 201°C for the 0.6°C/s cooling rate to 212°C at 2.4°C/s cooling rate.

Thermal analysis of MC MgAl12Zn1 revealed that the solidification process of material cooled at 0.6°C/s started at 583.01°C (Table 9). The next change on the first derivative curve, at 432.55°C was observed and corresponded to the nucleation of the α(Mg)-β(Mg-$Mg_{17}Al_{12}$) eutectic. The cooling curve for the MC MgAl12Zn1 alloy that solidified under at 1.2°C/s solidification rate started to solidify at 582.4°C and finished at 414.03°C. The nucleation of the α(Mg)-β(Mg-$Mg_{17}Al_{12}$) eutectic was observed at 436.05°C. The non-equilibrium liquidus temperature of MC MgAl12Zn1 alloy that solidified under a 2.4°C/s (Figure 26) was found approximately at 592.28°C. A further decrease in the temperature resulted in nucleation of the α(Mg)-β(Mg-$Mg_{17}Al_{12}$) eutectic at 441.87°C. The solidification process finished approximately at 415.42°C. Liquidus temperature and beginning of nucleation of α(Mg)-β(Mg-$Mg_{17}Al_{12}$) eutectic increases with cooling rate increase. The opposite way is for solidus temperature. Cooling rate increases cause solidus temperature decreases, resulting from widening the solidification range from 163°C to 177°C.

Table 9.
Non-equilibrium thermal characteristics of the MC MgAl12Zn1 alloy test samples obtained in the solidification process at 0.6°C/s, 1.2°C/s and 2.4°C/s solidification rates

Characteristic point	Solidification rates [°C/s]		
	0.6	1.2	2.4
	Temp. [°C]	Temp. [°C]	Temp. [°C]
I	583.01± 9.18	582.4±1.98	592.28±4.64
VII	432.55± 0.64	436.05±0.83	441.87±2.24
X	420.07±2.97	414.03±3.84	415.42±0.93

3.2. Laser treatment

A view of the MCMgAl12Zn1, MCMgAl9Zn1, MCMgAl6Zn1, MCMgAl3Zn1 cast magnesium alloys face weld after laser treatment with carbides and aluminium oxide were shown in Fig. 27-36. Influence of process parameters like laser power and used powders on shape and surface topography was observed. The front view after laser treatment using TiC and WC powders is regular with flat surface (Figs. 27, 28). When VC was used, the front view is characterised by flat surface, however the surface layer is discontinuous (Figs. 29, 30).

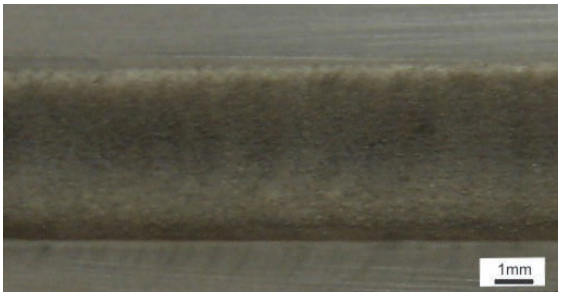

Fig. 27. A view of the MCMgAl3Zn1 cast magnesium alloy face weld after laser treatment with TiC, scan rate: 0.75 [m/min], laser power: 1.2 [kW]

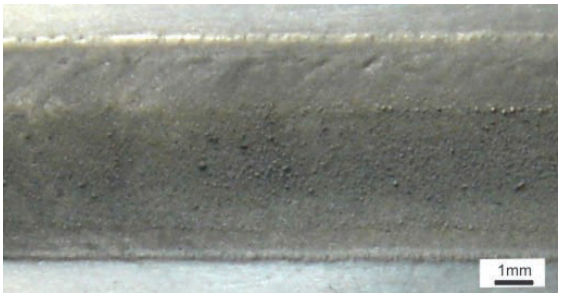

Fig. 28. View of the MCMgAl12Zn1 cast magnesium alloy face weld after laser treatment with WC, scan rate: 0.75 [m/min], laser power: 2.0 [kW]

Fig. 29. View of the MCMgAl12Zn1 cast magnesium alloy face of weld after laser treatment with VC, scan rate: 0.75 [m/min], laser power: 1.6 [kW]

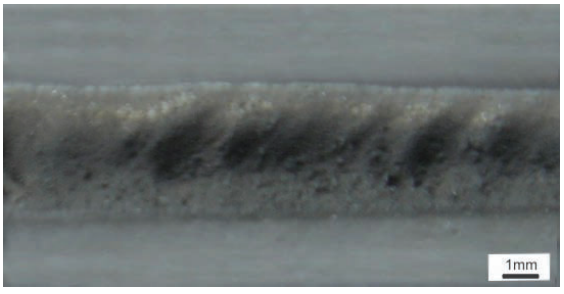

Fig. 30. View of the MCMgAl12Zn1 cast magnesium alloy face weld after laser treatment with VC, scan rate: 0.75 [m/min], laser power: 1.6 [kW]

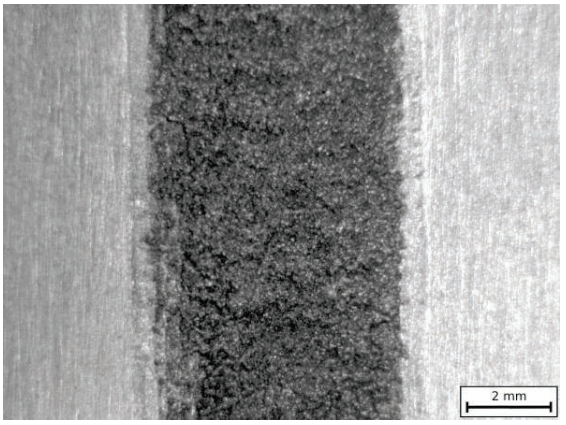

Fig. 31. View of the MCMgAl9Zn1 cast magnesium alloy face weld after laser treatment with SiC, scan rate: 0.75 [m/min], laser power: 2.0 [kW]

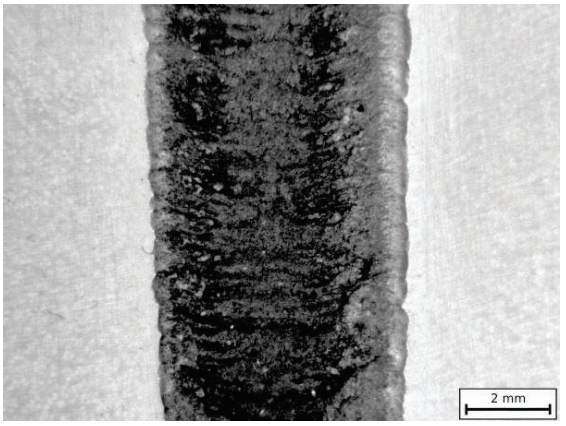

Fig. 32. View of the MCMgAl9Zn1 cast magnesium alloy face weld after laser treatment with NbC, scan rate: 0.25 [m/min], laser power: 2.0 [kW]

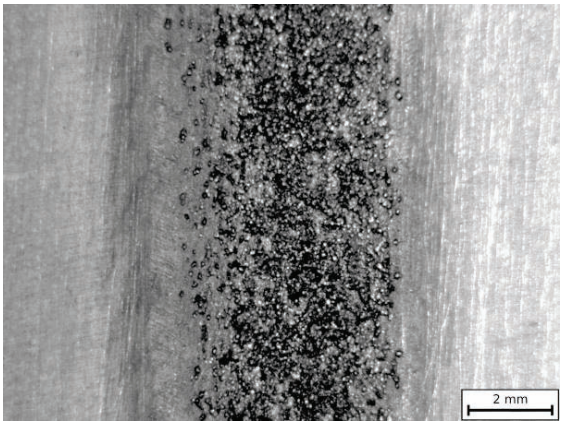

Fig. 33. View of the MCMgAl9Zn1 cast magnesium alloy face weld after laser treatment with Al2O3, scan rate: 0.50 [m/min], laser power: 2.0 [kW]

The magnesium alloys after laser treatment with SiC particles are characterised by convexity of remelting zone over base surface (Fig. 31).

Surface layer of cast magnesium alloys after laser treatment with NbC is characterised by irregular surface with material fashes, whereas Al_2O_3 is characterised by small hollow in the central area of bead face for laser power 2.0 kW (Fig. 32, 33).

Investigations reveal that laser power is increased by constant beam scanning rate and has influence on size of the area, where structural changes in the surface layer of the Mg-Al-Zn alloys occur.

Metallographic examinations revealed occurrence of several zones after laser alloying: alloyed zone (AZ), heat affected zone (HAZ) and substrate material in all the investigated cases. The shape and thickness of these zones are depending on laser power and scan rate. Results of the metallographic examinations show that the structure of material solidifying after laser remelting is characterised by occurrence of areas with diversified morphology, what is connected with crystallisation of the magnesium alloys. As a result of laser alloying, the defect-free structure is developed by the clearly state grain refinement (Fig. 34-43). Examinations carried out on the scanning electron microscope confirmed occurrence of the zonal structure in the surface layer in the investigated casting magnesium alloys (Fig. 34-43).

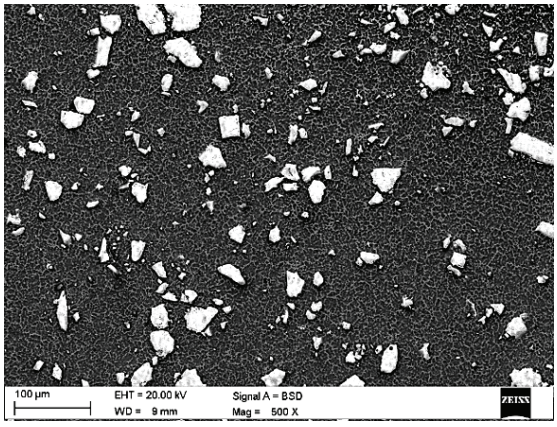

Fig. 34. Scanning electron microscope micrograph of laser modified surface of MCMgAl9Zn1 alloy with TiC particles of the central modified zone, scan rate: 0.75 [m/min], laser power: 1.6 [kW]

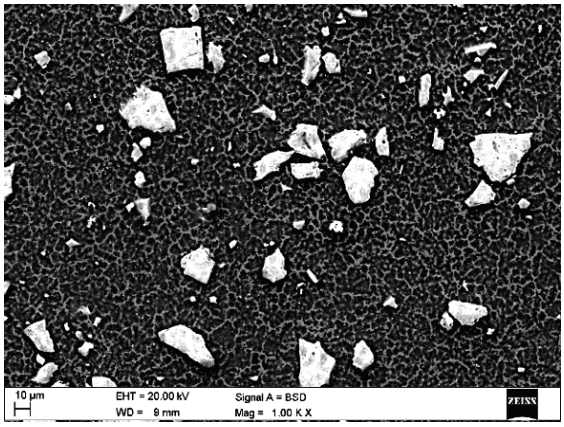

Fig. 35. Scanning electron microscope micrograph of laser modified surface of MCMgAl9Zn1 alloy with TiC particles of the central modified zone, scan rate: 0.75 [m/min], laser power: 1.6 [kW]

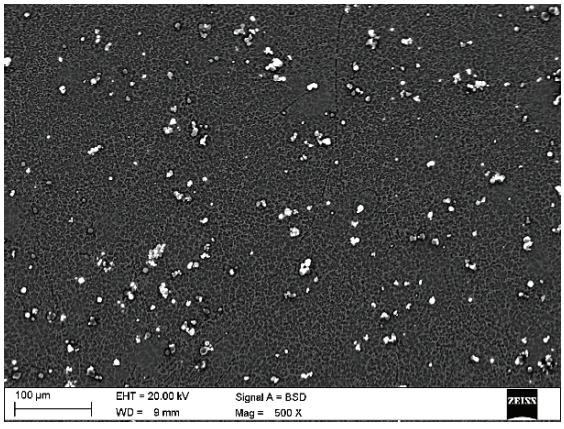

Fig. 36. Scanning electron microscope micrograph of laser modified surface of MCMgAl12Zn1 alloy with WC particles of the central modified zone, scan rate: 0.75 [m/min], laser power: 2.0 [kW]

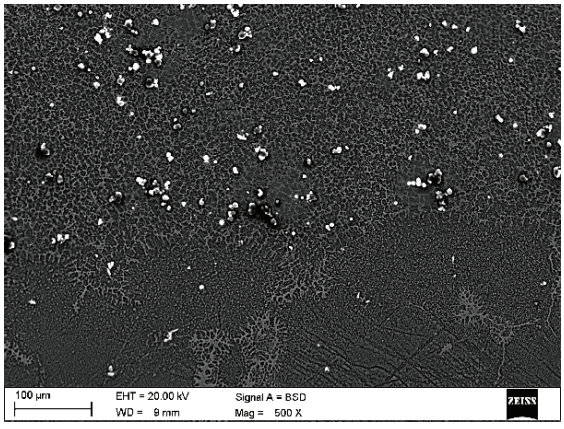

Fig. 37. Scanning electron microscope micrograph of laser modified surface of MCMgAl12Zn1 alloy with WC particles at the interface between the modified zone and substrate, scan rate: 0.75 [m/min], laser power: 2.0 [kW]

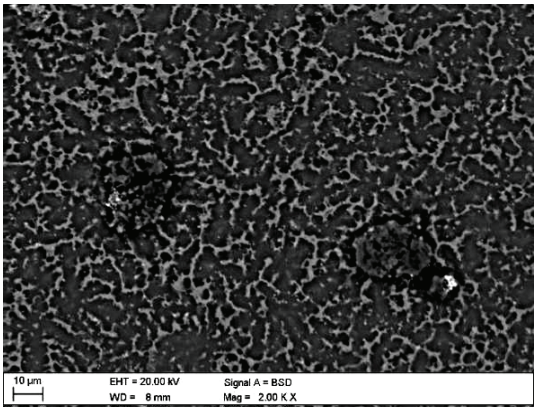

Fig. 38. Scanning electron microscope micrograph of laser modified surface of MCMgAl12Zn1 alloy with VC particles of the central modified zone, scan rate: 0.75 [m/min], laser power: 1.6 [kW]

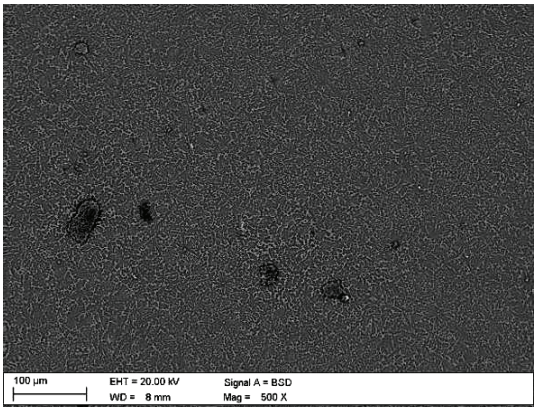

Fig. 39. Scanning electron microscope micrograph of laser modified surface of MCMgAl12Zn1 alloy with VC particles of the central modified zone, scan rate: 0.75 [m/min], laser power: 1.6 [kW]

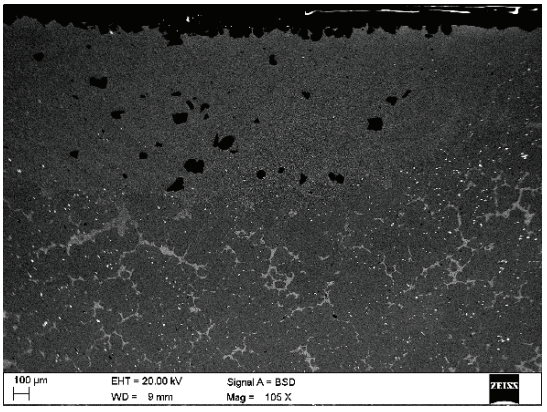

Fig. 40. Scanning electron microscope micrograph of laser modified surface of the MCMgAl12Zn1 with Al_2O_3 particle of the top surface of the coating, scan rate: 0.75 m/min, laser power: 1.6 [kW]

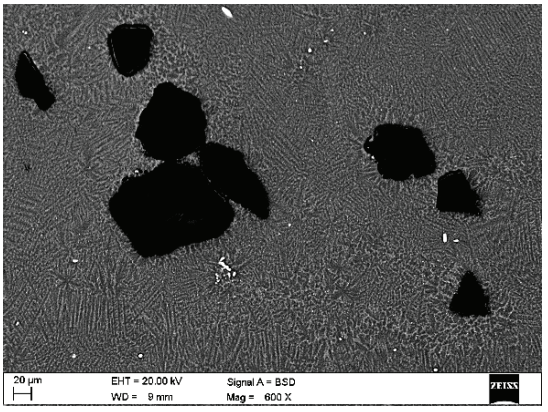

Fig. 41. Scanning electron microscope micrograph of laser modified surface of the MCMgAl12Zn1 alloy with Al_2O_3 particles of the central modified zone, scan rate: 0.50 [m/min], laser power: 1.6 [kW]

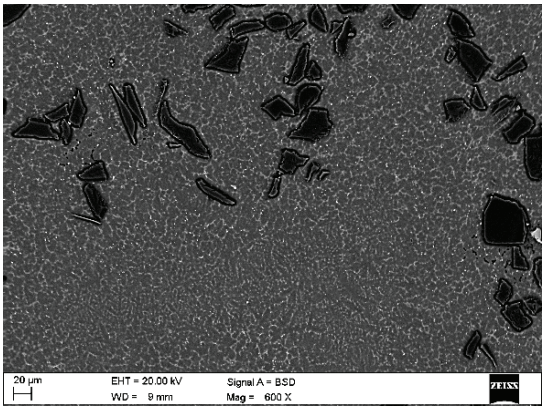

Fig. 42. Scanning electron microscope micrograph of laser modified surface of the MCMgAl9Zn1 alloy with SiC particles of the central modified zone, scan rate: 0.75 [m/min], laser power: 2.0 [kW]

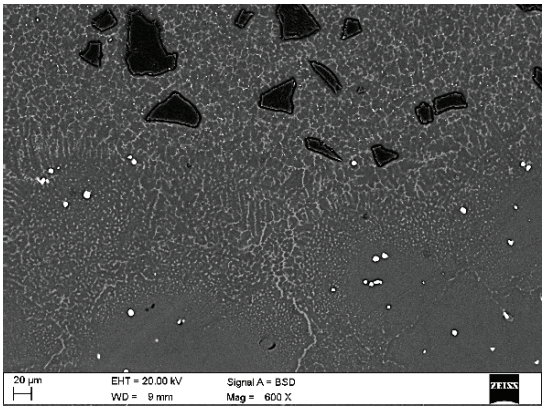

Fig. 43. Scanning electron microscope micrograph of laser modified surface of the MCMgAl9Zn1 alloy with SiC particles at the interface between the modified zone and the substrate, scan rate: 0.75 [m/min], laser power: 2.0 [kW]

It was found based on roughness measurement results of the cast magnesium alloys after laser treatment with titanium, tungsten, vanadium, silicon carbides and oxide aluminium that regardless of the ceramic powder employed the roughness of surface layers obtained by remelting the Mg-Al-Zn magnesium alloys with the laser beam using the power within 1.2 - 2.0 kW range, it grows in comparison with the prepared substrate and is within Ra = 6.4 – 42.5 µm range. Roughness growth occurs along with the laser power increase and aluminium concentration in the alloy. The MCMgAl9Zn1 alloy is an exception, as after alloying with TiC powder the surface roughness decreases along with the growing laser power.

Roughness of the surface layer treatment varied with laser power and also scan rate.

The effect of alloying conditions (laser power, alloying feed rate) with the TiC powder and substrate type on roughness and its growth was described with the regression function.

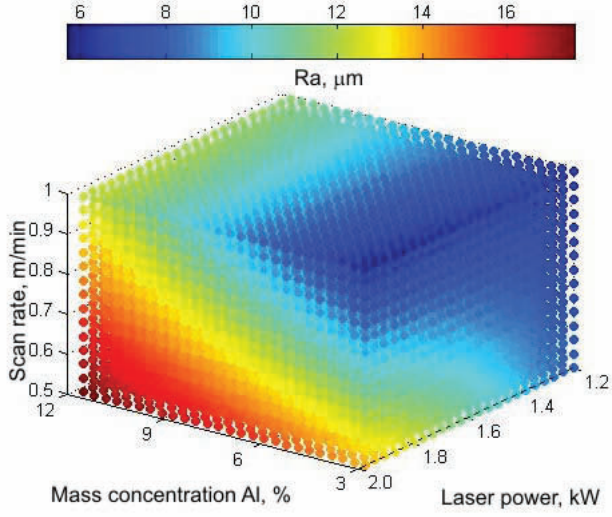

Fig. 44 Graph of the regression function showing dependence of roughness on aluminium concentration (wt. %), laser power and scan rate for laser treatment with TiC

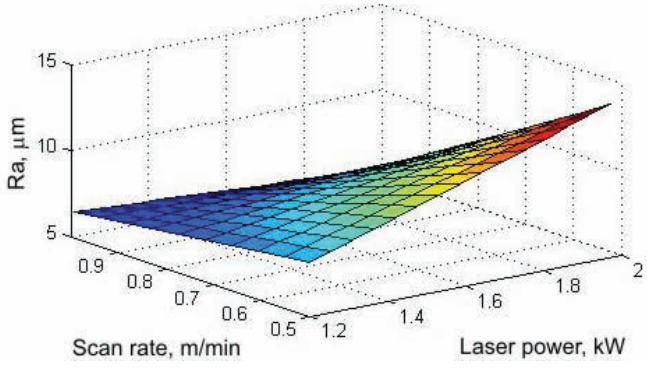

Fig. 45. Graph of the regression function showing dependence of roughness on laser power and scan rate for the EN-MCMgAl3Zn1 after laser treatment with TiC powder

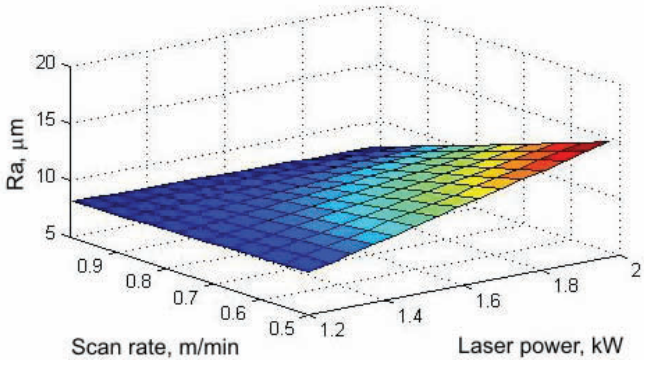

Fig. 46. Graph of the regression function showing dependence of roughness on laser power and scan rate for the EN-MCMgAl6Zn1 after laser treatment with TiC powder

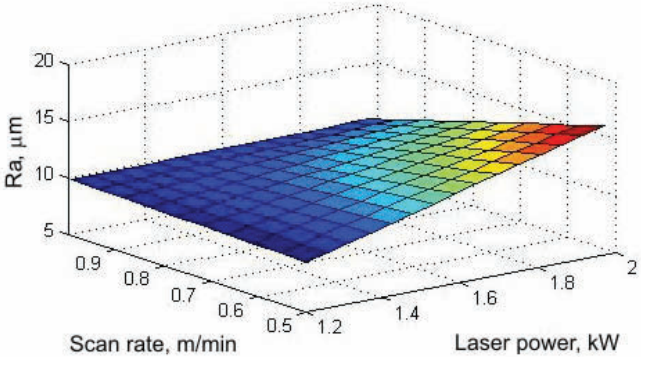

Fig. 47. Graph of the regression function showing dependence of roughness on laser power and scan rate for the EN-MCMgAl9Zn1 after laser treatment with TiC powder

Figs. 44 and 51 shows the graph of the regression function indicating interdependence of roughness increment measurement and aluminium mass concentration, laser power and scan rate. Magnesium alloys after laser treatment at laser power 2.0 kW and scan rate 0.5 m/min are characterised by maximum roughness Ra. Roughness is decreased when the laser power and constant scan rate and powder feed rate increase. MCMgAl9Zn1 and MCMgAl12Zn1 alloys after laser treatment with VC powder and 2.0 kW laser power are characterised by the lowest roughness suitably 4.0 and 5.6 µm (Fig. 49). Maximum value of roughness Ra equalling 42.5 µm was measured for MCMgAl9Zn1 alloy surface after laser treatment with SiC powder and 1.2 kW laser power (Figs. 51-55). Mg-Al-Zn alloys after laser treatment with TiC powder are characterised by roughness in the range from 6.4 to 13.9 µm (Figs. 44-48). In a case of WC powder laser treatment, the highest value of roughness was measured for 1.2 kW laser power and constant scan rate equal 0.75 m/min and the maximum roughness value 25.4 µm was measured for MCMgAl3Zn1 alloy. For all laser treatment parameters with NbC powder and for VC powder and MCMgAl6Zn1 alloy roughness measurements were not possible, because measuring range was too low (to 150 µm). Surface irregularity increase after laser treatment is connected

with melted alloy fluctuation that is produced by a change of surface tension and alloying material absorption of laser radiation energy.

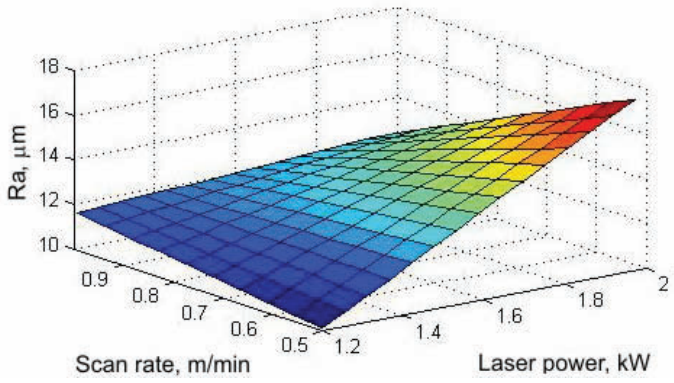

Fig. 48. Graph of the regression function showing dependence of roughness on laser power and scan rate for the EN-MCMgAl12Zn1 after laser treatment with TiC powder

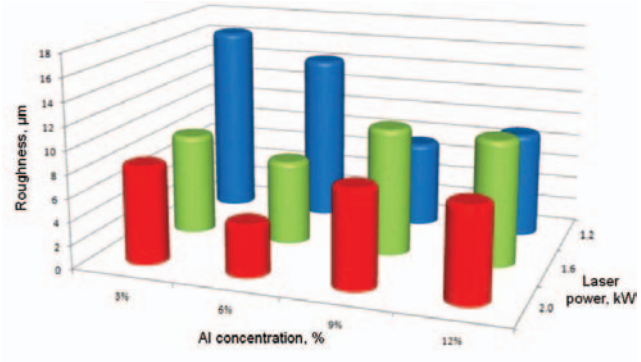

Fig. 49. Diagram of dependence of roughness on laser power and aluminium concentration (wt. %) magnesium alloys after laser treatment with WC powder and scan rate 0.75 m/min

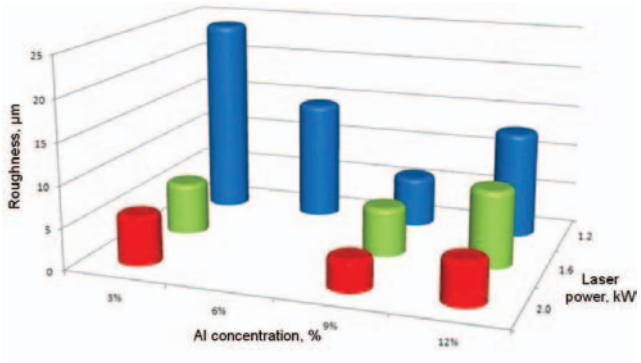

Fig. 50. Diagram of dependence of roughness on laser power and aluminium concentration (wt. %) magnesium alloys after laser treatment with VC powder and scan rate 0.75 m/min

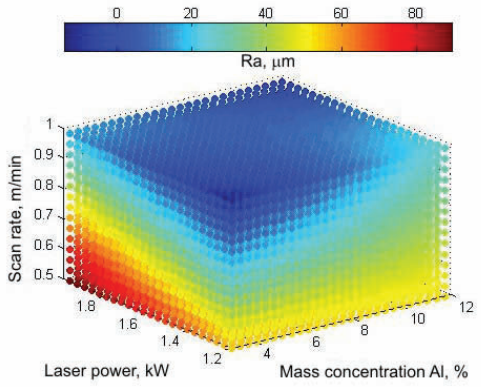

Fig. 51. Graph of the regression function showing dependence of roughness on aluminium concentration (wt. %), laser power and scan rate for laser treatment with SiC

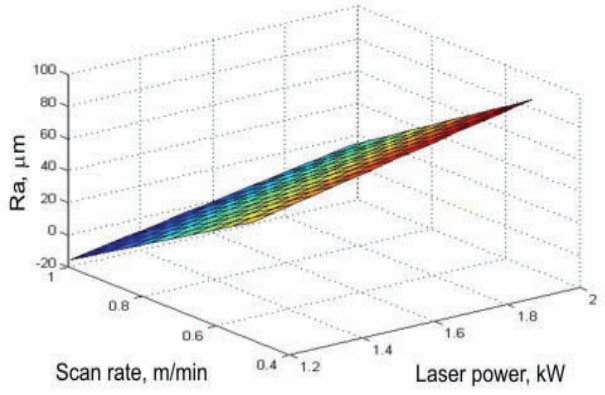

Fig. 52. Graph of the regression function showing dependence of roughness on laser power and scan rate for the EN-MCMgAl3Zn1 after laser treatment with SiC powder

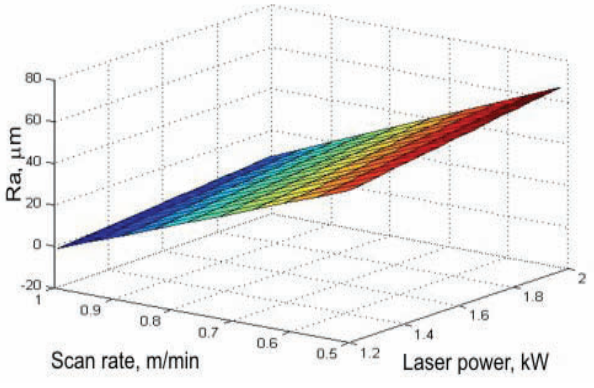

Fig. 53. Graph of the regression function showing dependence of roughness on laser power and scan rate for the EN-MCMgAl6Zn1 after laser treatment with SiC powder

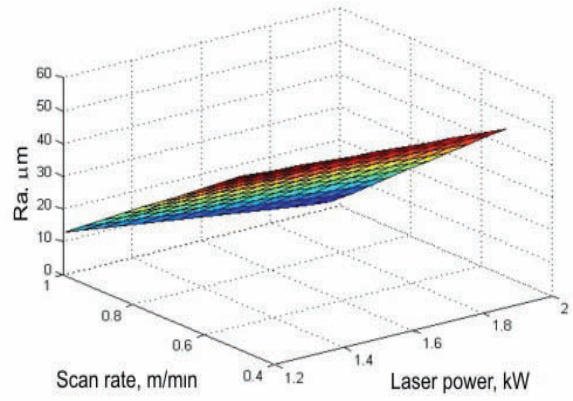

Fig. 54. Graph of the regression function showing dependence of roughness on laser power and scan rate for the EN-MCMgAl9Zn1 after laser treatment with SiC powder

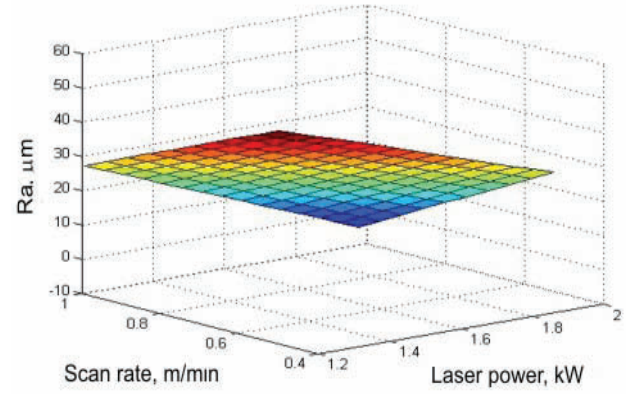

Fig. 55. Graph of the regression function showing dependence of roughness on laser power and scan rate for the EN-MCMgAl12Zn1 after laser treatment with SiC powder

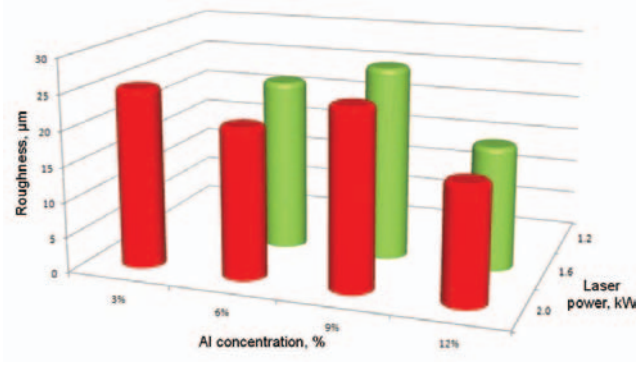

Fig. 56. Diagram of dependence of roughness on laser power and aluminium concentration (wt. %) magnesium alloys after laser treatment with Al_2O_3 powder and scan rate 0.5 m/min

Moreover, on the basis of neural network model, graphs of laser power, aluminium concentration and alloying powder type dependence on roughness of surface after laser treatment were developed (Figs. 57–61).

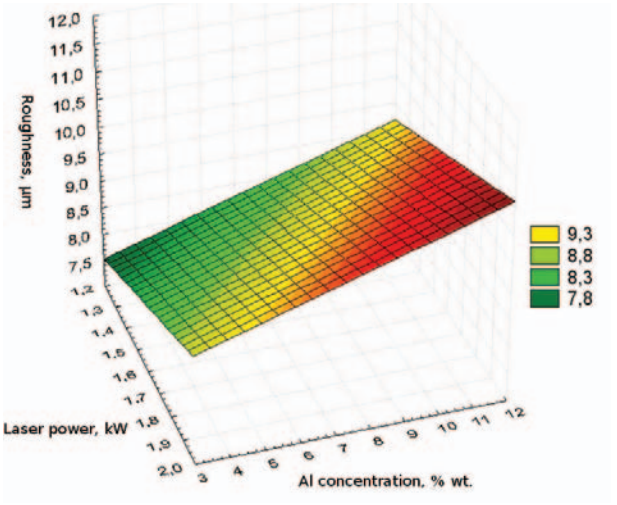

Fig. 57. Simulation of the laser power and aluminium concentration (wt. %) influence on roughness of the cast magnesium alloys after laser treatment with TiC and scan rate 0.75 m/min

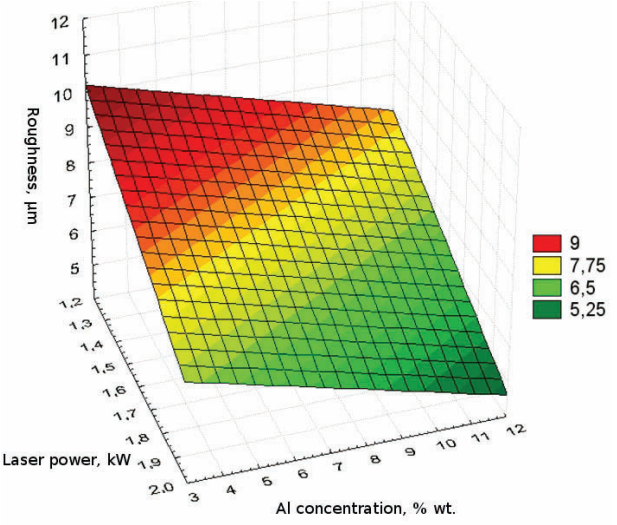

Fig. 58. Simulation of the laser power and aluminium concentration (wt. %) influence on roughness of the cast magnesium alloys after laser treatment with VC and scan rate 0.75 m/min

Results show that the lowest roughness is achieved for MCMgAl12Zn1 alloyed VC and WC powders with 2.0 kW laser power and 0.75 m/min scan rate. Discrepancy of correlation between neural network and regression function results for alloys after laser treatment with SiC powder comes from different interpretation of input data for laser treatments without melting g-Al-Zn alloys surfaces and cases measurements over the measurement range.

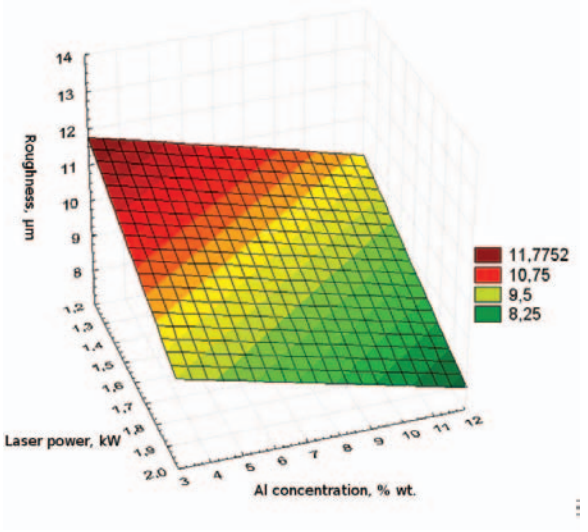

Fig. 59. Simulation of the laser power and aluminium concentration (wt. %) influence on roughness of the cast magnesium alloys after laser treatment with WC and scan rate 0.75 m/min

4. Conclusions

The result of the Metallographic examinations made on the optical and scanning electron microscope confirm that the investigated magnesium cast alloys MCMgAl12Zn1, MCMgAl9Zn, MCMgAl6Zn1, MCMgAl3Zn are characterised by a microstructure of solid solution α constituting the alloy matrix as well as the β - $Mg_{17}Al_{12}$ discontinuous intermetallic phase in the form of plates located mostly at grain boundaries. Moreover, in the vicinity of the β intermetallic phase precipitations of the needle eutectics appear (α + β). The applied ageing process after the solution heat treatment caused a release of the β phase at grain boundaries as well as in the form of quasi-eutectic locations. In the structure of the material, the parallel twinned crystals extending along the whole grain were revealed.

Derivative thermo-analysis performed allowed to achieve several representative cooling, crystallization and calorimetric curves with characteristics points of crystallisation process for MC MgAl9Zn1 alloy which were presented in Fig. 4, 5. Description of characteristics points obtained from thermal-derivative analysis was presented in Table 4 and made it possible to get better understanding of the thermal processes occurred during crystallisation kinetics of the investigated Mg alloys.

It was found, based on roughness measurement results of the casting magnesium alloys after laser treatment with the titanium, tungsten, vanadium, silicon carbides and oxide aluminium, that regardless of the ceramic powder employed in roughness of surface layers obtained by remelting the Mg-Al-Zn, Magnesium alloys with the laser beam using power within 1.2 - 2.0 kW range grow in comparison with the prepared substrate and they are within the Ra = 6, 4 - 42, 5 µm range. Moreover, on the basis of neural network model, graphs of laser power, aluminium concentration and alloying powder type dependence on roughness of surface after laser treatment were developed (Figs. 57–61). Results show that the lowest roughness is achieved for MCMgAl12Zn1 alloyed VC and WC powders at 2.0 kW laser power and 0.75 m/min scan rate.

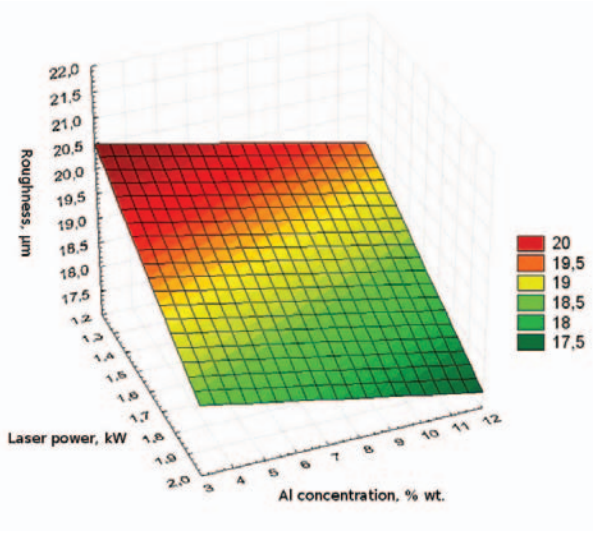

Fig. 60. Simulation of the laser power and aluminium concentration (wt. %) influence on roughness of the cast magnesium alloys after laser treatment with SiC and scan rate 0.75 m/min

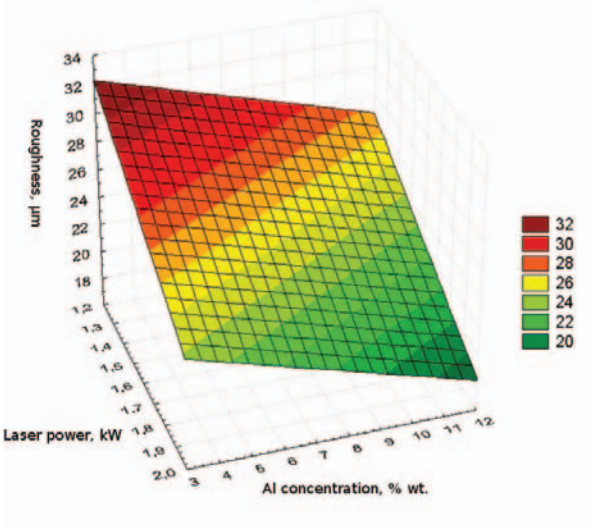

Fig. 61. Simulation of the laser power and aluminium concentration (wt. %) influence on roughness of the cast magnesium alloys after laser treatment with Al_2O_3 and scan rate 0.5 m/min

Acknowledgements

The paper has been realised in relation to the project POIG.01.01.01-00-023/08 entitled “Foresight of surface properties formation leading technologies of engineering materials and biomaterials” FORSURF, co-founded by the European Union from financial resources of European Regional Development Found and headed by Prof. L.A. Dobrzański.

INNOVATIVE ECONOMY
NATIONAL COHESION STRATEGY

FORSURF

EUROPEAN UNION
EUROPEAN REGIONAL
DEVELOPMENT FUND

References

[1] K.U. Kainer: Magnesium – Alloys and Technology, Wiley-VH, Weinheim, Germany, 2003.
[2] H. Friedrich, S. Schumann: Research for a ”New age of magnesium in the automotive industry”’, Journal of Materials Processing Technology, 117 (2001) 276-281.
[3] A. Fajkiel, P. Dudek, G. S□□k-Sas, Foundry engineering XXI c. Directions of metallurgy development and light alloys casting, Publishers Institute of Foundry engineering, Krakow 2002.
[4] X. Ming-Xu, Z. Hong-Xing, Y. Sen, L. Jian-Guo: Recrystallization of preformed AZ91D magnesium alloys in the semisolid state, Materials and Design, 26 (2005) 343-349.
[5] E.F. Horst, B.L. Mordike: Magnesium Technology. Metallurgy, Design Data, Application, Springer-Verlag, Berlin Heidelberg 2006.
[6] Kiełbus, T. Rzychoń, R. Cibis, Microstructure of AM50 die casting magnesium alloy, Journal of Achievements in Materials and Manufacturing Engineering, 18 (2006) 135-138.
[7] J. Zhang, Z.X. Guo, F. Pan, Z. Li, X. Luo, Effect of composition on the microstructure and mechanical properties of Mg-Zn-Al alloys, Materials Science & Engineering A, 456 (2007) 43-51.
[8] L.A. Dobrzański, T. Tański, L. Cížek, Z. Brytan, Structure and properties of the magnesium casting alloys, Journal of Materials Processing Technology, 192-193 (2007) 567-574.
[9] T. Tański, L.A. Dobrzański, L. Cížek, Influence of heat treatment on structure and properties of the cast magnesium alloys, Journal of Advanced Materials Research, 15-17 (2007) 491-496.
[10] S.G. Shabestari, M. Malekan, Thermal analysis study of the effect of the cooling rate on the microstructure and solidification parameters of 319 aluminum alloy, Canadian Metallurgical Quarterly 44(3) (2005) 305-312.
[11] L. Backuerud, G. Chai, J Tamminen, Solidification characteristics of aluminum alloys Vol.2 Foundry Alloys, AFS Skanaluminium, Stockholm, Sweden 1990.
[12] L.A. Dobrzanski, W. Kasprzak, M. Kasprzak, J.H. Sokolowski, A Novel Approach to the Design and Optimization of Aluminum Cast Component Heat Treatment Processes Using Advanced UMSA Physical Simulations, Journal of Achievements in Materials and Manufacturing Engineering 24/2 (2007) 139-142.
[13] D. Emadi, L.V. Whiting, S. Nafisi, R. Ghomashchi, Applications of thermal analysis in quality control of solidification processes, Journal of Thermal Analysis and Calorimetry 81 (2005) 235-242.
[14] L.A. Dobrzanski, W. Kasprzak, J. Sokolowski, R. Maniara, M. Krupinski, Applications of the derivation analysis for assessment of the ACAlSi7Cu alloy crystallization process cooled with different cooling rate, Proceedings of the 13th Scientific International Conference on Achievements In Mechanical and Materials Engineering, AMME’2005, Gliwice - Wisla, Poland, 147-150, 2005.
[15] J.H. Sokolowski, M.B. Djurdjevic, Ch.A. Kierkus, D.O. Northwood, Improvement of 319 aluminium alloy casting durability by high temperature solution treatment, Journal of Materials Processing Technology 109 (2001) 174-180.
[16] H. Yamagata, H. Kurita, M. Aniolek, W. Kasprzak, J.H. Sokolowski, Thermal and metallographic characteristics of the Al-20% Si high-pressure die casting alloy for monolithic cylinder blocks, Journal of Materials Processing Technology 199 (2008) 84-90.
[17] W.T. Kierkus, J.H. Sokolowski, Recent Advances in CCA:A new method of determining baseline equation, AFS Transactions 66 (1999) 161-167.
[18] M.B. Djurdjevis, W.T. Kierkus, G.E. Byczynski, T.J. Stockwell, J.H. Sokolowksi, Modelling of fraction solid for 319 aluminum alloy, AFS Transactions 1999(14) 173-179.
[19] “Method and Apparatus for Universal Metallurgical Simulation and Analysis” – United States Patent, Patent No.: US 7,354,491 B2, Date of Patent: Apr. 8.
[20] W. Kasprzak, J.H. Sokolowski, W. Sahoo, L.A. Dobrzanski, Thermal and structural characteristics of the AZ50 magnesium alloy, Journal of Achievements in Materials and Manufacturing Engineering 29/2 (2008) 179-182.
[21] H. Yamagata, W. Kasprzak, M. Aniolek, H. Kurita, J.H. Sokolowski, The effect of average cooling rates on the microstructure of the Al-20%Si high pressure die casting alloy used for monolithic cylinder blocks, Journal of Materials Processing Technology 203 (2008) 333-341.
[22] R. MacKay, M. Djurdjevic, J.H. Sokolowski, The effect of cooling rate on the fraction solid of the metallurgical reaction in the 319 alloy, AFS Transaction, 2000.
[23] Universal Metallurgical Simulator and Analyzer (UMSA) Platform for the Advanced Simulation of Melting and Solidification Processes, Software Information, 2002.
[24] L.A Dobrzanski, K. Labisz, M. Piec, A. Klimpel, Modelling of surface layer of the 31CrMoV12-18 tool steel using HPDL laser for alloying with TiC powder, Journal of Achievements in Materials and Manufacturing Engineering 24/2 (2007) 27-34.
[25] D. Dube, M. Fiset, A. Couture, I. Nakatsugawa, Characterization and performance of laser melted AZ91D and AM60B, Materials Science and Engineering A299 (2001) 38-45.
[26] F. Vollertsen, K. Partes, J. Meijer, State of the art of Laser Hardening and Cladding, Proceedings of the 3th International WLT-Conference on Lasers in Manufacturing 2005, Munich.
[27] L. Kukiełka: Bases for engineering studies, Polish Scientific Publishers, Warsaw 2002